

Convection and Differential Rotation Properties of G & K Stars Computed with the ASH Code

Sean P. Matt^{1*}, Olivier Do Cao¹, Benjamin P. Brown², and Allan Sacha Brun¹

¹ Laboratoire AIM Paris-Saclay, CEA/Irfu Université Paris-Diderot CNRS/INSU, 91191 Gif-sur-Yvette, France

² Department of Astronomy and Center for Magnetic Self Organization in Laboratory and Astrophysical Plasmas, University of Wisconsin, 475 N. Charter St., Madison WI 53706, USA

Received 6 Oct 2011, accepted 17 Nov 2011

Published online later

Key words convection – hydrodynamics – Stars: interiors – Stars: rotation – turbulence

The stellar luminosity and depth of the convective envelope vary rapidly with mass for G- and K-type main sequence stars. In order to understand how these properties influence the convective turbulence, differential rotation, and meridional circulation, we have carried out 3D dynamical simulations of the interiors of rotating main sequence stars, using the anelastic spherical harmonic (ASH) code. The stars in our simulations have masses of 0.5, 0.7, 0.9, and 1.1 M_{\odot} , corresponding to spectral types K7 through G0, and rotate at the same angular speed as the sun. We identify several trends of convection zone properties with stellar mass, exhibited by the simulations. The convective velocities, temperature contrast between up- and downflows, and meridional circulation velocities all increase with stellar luminosity. As a consequence of the trend in convective velocity, the Rossby number (at a fixed rotation rate) increases and the convective turnover timescales decrease significantly with increasing stellar mass. The 3 lowest mass cases exhibit solar-like differential rotation, in a sense that they show a maximum rotation at the equator and minimum at higher latitudes, but the 1.1 M_{\odot} case exhibits anti-solar rotation. At low mass, the meridional circulation is multi-cellular and aligned with the rotation axis; as the mass increases, the circulation pattern tends toward a unicellular structure covering each hemisphere in the convection zone.

© 2011 WILEY-VCH Verlag GmbH & Co. KGaA, Weinheim

1 Introduction

The sun and sun-like stars with convection zones in their outer envelopes, have long been known to exhibit emission line and X-ray activity, associated with hot gas in chromospheres, transition regions, and coronae (e.g., Pizzolato et al., 2003; Strassmeier et al., 1990; Wright et al., 2011). Understanding this activity, and understanding how the solar case relates to the activity observed across the HR diagram is a long-standing puzzle. It is clear that the existence of hot gas above the photosphere is related to magnetic processes associated with the convection zone itself. The magnetic field of low-mass main sequence stars is generally believed to be generated by dynamo processes, which derive their properties from convective motions, differential rotation, and meridional circulations in the convection zones, as well as from the interaction between the convection zone and the radiative interior.

Recent observations, by either spectropolarimetry (e.g., Donati et al., 2003), doppler imaging (e.g., Barnes et al., 2005), or monitoring of various activity indicators (e.g., Baliunas et al., 1995; Donahue et al., 1996; Lovis et al., 2011; Oláh et al., 2009; Saar & Brandenburg, 1999), show that solar-like stars possess activity cycles and differential rotation, analogous to the sun. Solar analogues are even starting to be discovered (Petit et al., 2008).

In order to gain a better theoretical understanding of how convective properties depend upon stellar parameters, we carry out 3D numerical dynamical simulations of convective envelopes of solar-like stars. As a first step, we model here the convective regions only, neglecting the effects of the interface region with a radiative envelope, and restrict ourselves to relatively slow (solar) rotation rates. Specifically, we simulate the convection dynamics for 4 main sequence stars with masses of 0.5, 0.7, 0.9, and 1.1 solar masses, spanning spectral types G0 to K7. This mass interval exhibits a large range of the physical properties of convective envelopes (such as the depth, physical size, mass, and density), as well as in the overall stellar luminosity transported by convection. These types of stars are also targets for asteroseismic studies (e.g., Verner et al., 2011), which have the potential to give precise measurements of stellar properties for large numbers of stars. The goal here is to determine how the convection, differential rotation, and meridional circulation is influenced by stellar mass, and to see if general trends or scaling laws can be extracted that will guide a deeper understanding of the inner hydrodynamics of these stars. The present study lays the groundwork for later studies to consider (e.g.) faster rotation rates, convection-radiation zone interface dynamics, and the dynamo generation of magnetic fields in stars in this mass range.

Section 2 contains a description of our simulation method and presents a comparison of the overall structures of each star. Section 3 describes the main results of our 3D simula-

* Corresponding author: e-mail: sean.matt@cea.fr

tions, focusing on both the convective turbulence properties, as well as the differential rotation and meridional circulation flows. A summary and brief discussion is contained in section 4.

2 Simulation method

We use the anelastic spherical harmonic (ASH) code (Clune et al., 1999) to compute the 3-dimensional and turbulent flows in convectively unstable stellar envelopes. This code has been extensively tested and used for computing several aspects of the solar interior (e.g., Browning et al., 2006; Brun et al., 2004; Brun & Toomre, 2002; DeRosa et al., 2002; Miesch et al., 2006), rapidly rotating young stars (Ballot et al., 2007; Brown, 2009; Brown et al., 2008, 2011), the convective cores of massive stars (Browning et al., 2004a,b; Featherstone et al., 2009), fully convective low mass stars (Browning, 2008), red giant stars (Brun & Palacios, 2009), and pre-main-sequence stars (Bessolaz & Brun, in this volume; Bessolaz & Brun, 2011). We briefly describe the basic aspects of the code here, but the reader can find further details of the code in those previous works (see especially, Brun et al., 2004; Clune et al., 1999).

The code solves the fluid equations, under the anelastic approximation, in a computational domain consisting of a spherical shell and in a rotating reference frame. Under the anelastic approximation, sound waves are filtered out and assumed to have a negligible effect on the dynamics, in order to allow for a larger computational timestep. This approximation is appropriate (e.g.) in the interiors of stars because typical motions are highly sub-sonic. The thermodynamic variables are linearized with respect to a spherically symmetric background state with a density $\bar{\rho}$, pressure \bar{P} , temperature \bar{T} , and specific entropy \bar{S} and fluctuations about the background state of ρ , P , T , and S . The time-dependent equations describe the conservation of mass, momentum, and entropy expressed as

$$\nabla \cdot (\bar{\rho} \mathbf{v}) = 0, \quad (1)$$

$$\bar{\rho} \left(\frac{\partial \mathbf{v}}{\partial t} + (\mathbf{v} \cdot \nabla) \mathbf{v} + 2\Omega_0 \times \mathbf{v} \right) = -\nabla P + \rho \mathbf{g} - [\nabla \bar{P} - \bar{\rho} \mathbf{g}] - \nabla \cdot \mathcal{D}, \quad (2)$$

$$\begin{aligned} \bar{\rho} \bar{T} \frac{\partial S}{\partial t} + \bar{\rho} \bar{T} \mathbf{v} \cdot \nabla (\bar{S} + S) = \\ + \nabla \cdot [\kappa_r \bar{\rho} c_p \nabla (\bar{T} + T) + \bar{\rho} \bar{T} (\kappa \nabla S + \kappa_0 \nabla \bar{S})] \\ + 2\bar{\rho} \nu [e_{ij} e_{ij} - 1/3(\nabla \cdot \mathbf{v})^2], \end{aligned} \quad (3)$$

where $\mathbf{v} = (v_r, v_\theta, v_\phi)$ is the velocity in the rotating frame in spherical coordinates, $\Omega_0 = \Omega_0 \hat{\mathbf{e}}_z$ is the angular rotation rate of the reference frame, \mathbf{g} is the acceleration due to gravity, κ_r is the radiative diffusivity, and c_p is the specific heat at constant pressure. The term \mathcal{D} is the viscous stress tensor, with the components

$$\mathcal{D}_{ij} = -2\bar{\rho} \nu [e_{ij} - 1/3(\nabla \cdot \mathbf{v}) \delta_{ij}], \quad (4)$$

where e_{ij} is the strain rate tensor, and ν , κ , and κ_0 are effective eddy diffusivities. The code also uses a linearized equation of state,

$$\frac{\rho}{\bar{\rho}} = \frac{P}{\bar{P}} - \frac{T}{\bar{T}} = \frac{P}{\gamma \bar{P}} - \frac{S}{c_p}, \quad (5)$$

and the ideal gas law,

$$\bar{P} = \mathcal{R} \bar{\rho} \bar{T}, \quad (6)$$

where γ is the ratio of specific heats (we use $\gamma = 5/3$), and \mathcal{R} is the gas constant. For all 4 stars in our study, the luminosity has reached a value of more than 99.9% of the total stellar luminosity by the base of the convection zone, so we do not need to include any energy generation by nuclear burning within our computational domain.

We set up four different models in which the domain boundaries and stratification coincides with 1D models of the convection zones of main sequence stars with different masses. Section 2.1 describes the global properties of these stars, and sections 2.2 and 2.3 describe the initial and boundary conditions used in our ASH models, as well as the method for evolving the simulations to a fully-convective, statistical steady-state.

2.1 1D stellar structure

In order to define the background structure for our 3D models, we use the 1D stellar evolution code CESAM (Morel, 1997). With CESAM, we computed the evolution of four stars with masses of 0.5, 0.7, 0.9, and 1.1 M_\odot until the age of 4.6 Gyr. This age is approximately equal to that of the sun, so our cases can be compared with the many previous results of solar studies. Also, this age is appropriate for the slow (solar) rotation rates considered here. For all four stars, we assumed the same initial metallicity of $(X, Y, Z) \approx (0.71, 0.27, 0.02)$ and a mixing length parameter of 1.77, chosen to best represent the solar case. Table 1 lists the key global properties of our four stars, at the age of 4.6 Gyr, which are also graphically represented in Figures 1–3.

Figure 1 shows the total luminosity (solid line), as well as the effective temperature (dashed line) as a function of mass, for stars in the mass range of our models. The “X” symbols mark the values for the 4 stars modeled here, which are also listed in table 1. Also indicated on the plot are the approximate spectral types, corresponding to the effective temperature. The Figure demonstrates the steep rise in luminosity with mass expected for main sequence stars (the stars here approximately follow $L_* \propto M_*^{4.6}$), such that the 1.1 M_\odot star is 40 times more luminous than the 0.5 M_\odot star.

Figure 2 shows the photospheric radius R_* (upper solid line) and the radial location of the base of the convection zone R_{cz} (lower solid line) as a function of mass. The stellar radius is strong function of stellar mass in the plotted range, with the 1.1 M_\odot star being 2.8 times bigger than the 0.5 M_\odot star. The radial extent of the convection zones for these stars is represented by the region between the two

Table 1 Global properties of the 4 stars used in our ASH models, computed with the CESAM stellar evolution code and at an age of 4.6 Gyr. We adopt $M_{\odot} = 1.989 \times 10^{33}$ g, $R_{\odot} = 6.9599 \times 10^{10}$ cm, and $L_{\odot} = 3.846 \times 10^{33}$ erg s $^{-1}$.

Mass (M_{\odot})	Radius (R_{\odot})	L_* (L_{\odot})	T_{eff} (K)	SpT	M_{cz} (M_{\odot}, M_*)	R_{cz} (R_{\odot}, R_*)	$T(R_{\text{cz}})$ (K)	$\rho(R_{\text{cz}})$ (g cm $^{-3}$)
0.5	0.44	0.046	4030	K7	0.18, 0.36	0.25, 0.56	4.3×10^6	14
0.7	0.64	0.15	4500	K4/K5	0.079, 0.11	0.42, 0.66	3.0×10^6	2.1
0.9	0.85	0.55	5390	G8	0.042, 0.046	0.59, 0.69	2.6×10^6	0.51
1.1	1.23	1.79	6030	G0	0.011, 0.0100	0.92, 0.75	1.6×10^6	0.048

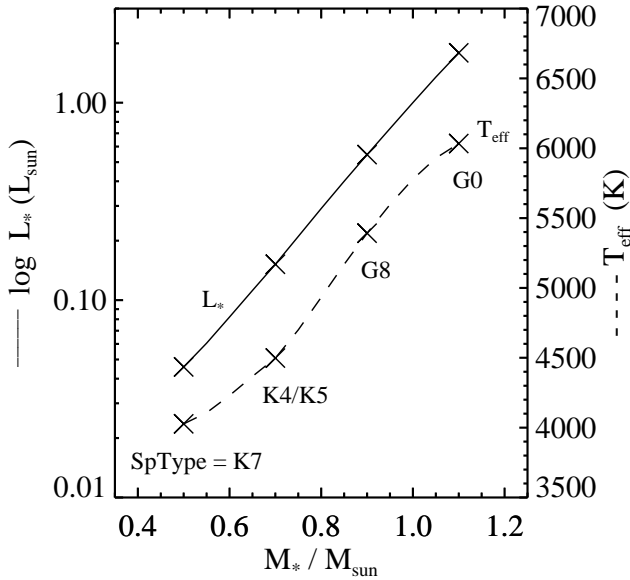


Fig. 1 Stellar luminosity in solar units (solid line, left scale) and effective temperature (dashed line, right scale) as a function of stellar mass, for the mass range spanned by our models, and as computed using the CESAM stellar evolution code. The “X” symbols indicate the values for the 4 stars used in our 3D ASH simulations. The approximate spectral types are also indicated next to each of these.

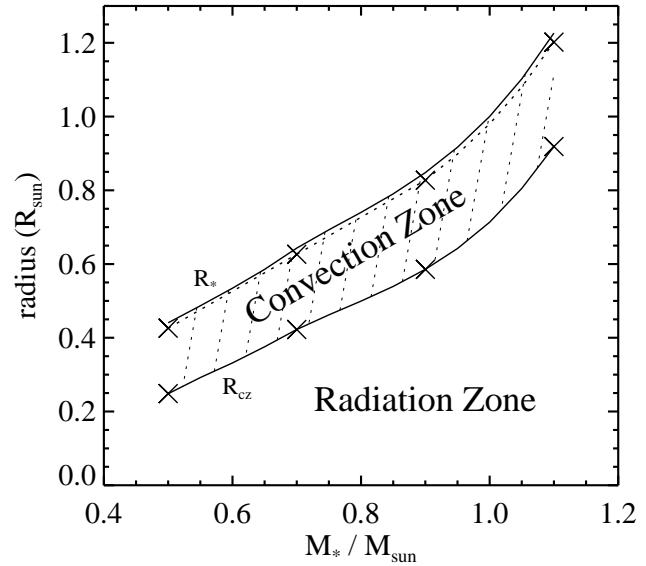


Fig. 2 Stellar radius (upper line) and radial location of the base of the convection zone (lower line) in solar units and as a function of stellar mass, as computed by the CESAM stellar evolution code. The convection zone exists between these two lines, while a convectively stable radiation zone lies below. The “X” symbols indicate the upper and lower radial boundaries of the computational domain used in our ASH simulations, for the 4 cases considered.

solid lines, and the region below contains a convectively stable radiation zone. It is clear that, in the mass range shown, the thickness of the convection zone increases slightly with increasing stellar mass. However, since the stellar radius increases more rapidly, the fractional size of the convection zone decreases with increasing mass. Thus, the convection zone thickness ranges from 44% to 25% of the stellar radius, for the 0.5 and 1.1 M_{\odot} stars, respectively (for the sun, this value is approximately 30%). The “X” symbols indicate the upper and lower boundaries of our 3D simulation domains for the 4 stars simulated (discussed below).

Figure 3 shows the extent of convection zones, expressed in mass coordinates and normalized to the mass of each star, as a function of stellar mass. The lines show the total mass enclosed by the stellar surface (upper line) and enclosed by the location of the base of the convective envelope (lower line). The amount of mass contained in the convection zone, M_{cz} , is the difference between these two lines and is listed in Table 1. It is clear that the convection zone mass is a

strong function of stellar mass in the range considered. Stars with slightly lower mass will be fully convective, while significantly more massive stars will not have convective envelopes. The convection zone mass varies from 36% to 1% of the stellar mass, for the 0.5 and 1.1 M_{\odot} stars, respectively (the solar value is approximately 3%). The “X” symbols indicate the simulation domain boundaries, expressed in mass coordinates, for the 4 stars simulated (discussed below).

The last two columns of table 1 show the temperature and the mass density at the base of the convection zone for each case. Although it is true that the temperature and density increases with mass at the stellar center ($R = 0$), these quantities decrease with increasing mass at the location of R_{cz} . In other words, for increasing stellar mass, the convection zone generally occupies a more tenuous and cooler outer layer of the star.

Table 2 Simulation parameters for each case. The number of radial, latitudinal, and longitudinal gridpoints are N_r , N_θ , and N_ϕ . The outermost radius of the simulated spherical shell is R_{out} , and $H_\rho(R_{\text{out}})$ is the density scale height there. The radial size of the domain is $L = R_{\text{out}} - R_{\text{cz}}$. The viscosity at R_{out} is ν_{top} and it varies in the domain with the inverse square root of the background density. All stars have a Prandtl number $P_r \equiv \nu/\kappa = 0.25$ and rotate at the solar rate, $\Omega_0 = 2.6 \times 10^{-6}$ rad/s, corresponding to a rotation period of $2\pi/\Omega_0 \approx 28$ days. Also listed are the Rayleigh number $R_a \equiv (-\partial\rho/\partial S)\Delta S g L^3/(\rho\nu\kappa)$, the Taylor number $T_a \equiv 4\Omega^2 L^4/\nu^2$, and the convective Rossby number $R_{oc} \equiv (R_a/T_a P_r)^{1/2}$, all evaluated at the midlevel of the domain.

Mass (M_\odot)	N_r, N_θ, N_ϕ	R_{out} (R_\odot, R_*)	$H_\rho(R_{\text{out}})$ (Mm)	L (Mm)	ν_{top} ($\text{cm}^2 \text{s}^{-1}$)	R_a	T_a	R_{oc}
0.5	257, 256, 512	0.43, 0.97	6.1	120	3.5×10^{11}	3.9×10^6	1.5×10^8	0.32
0.7	257, 256, 512	0.63, 0.97	6.3	140	2.0×10^{12}	6.0×10^5	8.1×10^6	0.54
0.9	257, 256, 512	0.83, 0.98	7.6	170	5.0×10^{12}	1.9×10^5	2.6×10^6	0.54
1.1	257, 256, 512	1.20, 0.98	8.6	200	2.0×10^{13}	3.6×10^4	3.2×10^5	0.67

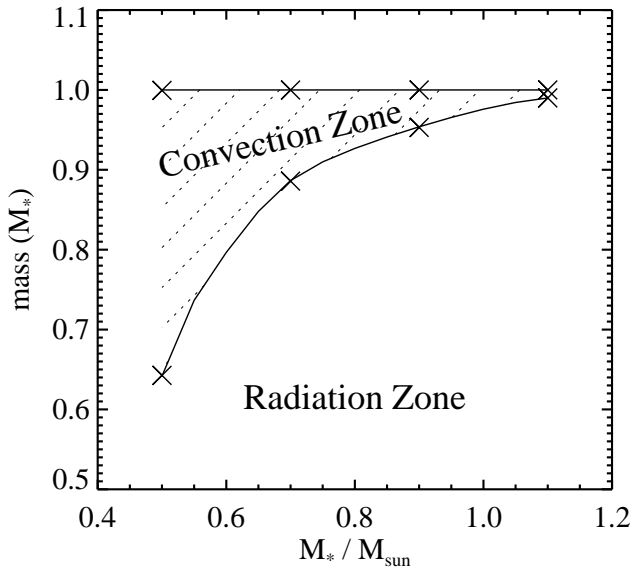


Fig. 3 Mass contained beneath the stellar surface (upper line) and location of the base of the convection zone (lower line) as a function of stellar mass, as computed by the CESAM stellar evolution code. The convection zone exists between these two lines, while a convectively stable radiation zone lies below. The “X” symbols indicate the upper and lower radial boundaries of the computational domain used in our ASH simulations, for the 4 cases considered.

2.2 Initial and boundary conditions for 3D simulations

We use the 1D stellar structure models described above for the spherically symmetric, initial conditions of the 3D ASH models. Table 2 lists the key properties of each of the 4 simulations. In the ASH models presented here, the domain consists of the stellar convection zone only. Thus, the lower radial boundary of our simulated spherical shells coincides with the base of the convection zone, R_{cz} , for each star (see table 1 and the lower row of “X” symbols in Figs. 2 and 3). We chose the location of the outer boundary such that the mass density there is a factor of 100 smaller than at the base of the convection zone. This places the outer boundary

somewhat below the photosphere of the star. The location of the outer boundary R_{out} is listed in table 2 and shown as the upper row of “X” symbols in and Figures 2 and 3.

In each of our 4 cases, the gravity (g) is taken directly from the corresponding CESAM model, and the entropy gradient ($\partial\tilde{S}/\partial r$) is initialized with a constant value equal to the (superadiabatic) entropy gradient in the middle of the convection zone in the CESAM model. The background thermodynamic variables ($\bar{\rho}$, \bar{P} , \bar{T} , and \bar{S}) are set according to this entropy gradient and to be in hydrostatic balance with the stellar gravity, while the fluctuating thermodynamic variables (ρ , P , T , and S) are initially zero. The initial entropy gradient and choice of diffusivities (see below) ensures that the initial state is convectively unstable and has a Rayleigh number near or above the critical Rayleigh number necessary for convection. The velocity in the rotating frame (v) is given an initial random perturbation, with negligible kinetic energy, in order to initiate convective motions.

For both the inner and outer boundaries, we use stress-free and impenetrable boundary conditions on the velocity and hold the entropy gradient fixed at the initial value. The radiative diffusivity κ_r is chosen so that the ASH model has the same radiative flux at all radii as the corresponding CESAM model. The initial stellar structure and boundary conditions ensure that the energy flux into the domain at the bottom of the convection zone (given entirely by the radiative flux) is constant in time. At the top of the domain, the density scale height becomes small (see table 2), and since this approximately determines the convection cell size scale, it becomes numerically challenging to resolve the convective motions there. Furthermore, the impenetrable boundary condition precludes any convective enthalpy flux from escaping the top of the domain. To address both of these issues we introduce a diffusive energy flux (the term proportional to κ_0 in eq. [3]) that is assumed to represent an unresolved and spherically symmetric enthalpy flux carried by small-scale convection near the top of the domain (hereafter “unresolved eddy flux”). In all 4 cases, we chose κ_0 so that this flux is negligible in the bulk of the convection zone, but increases as a smooth function near the outer boundary, such that the flux leaving the domain equals the stellar energy flux and is constant in time.

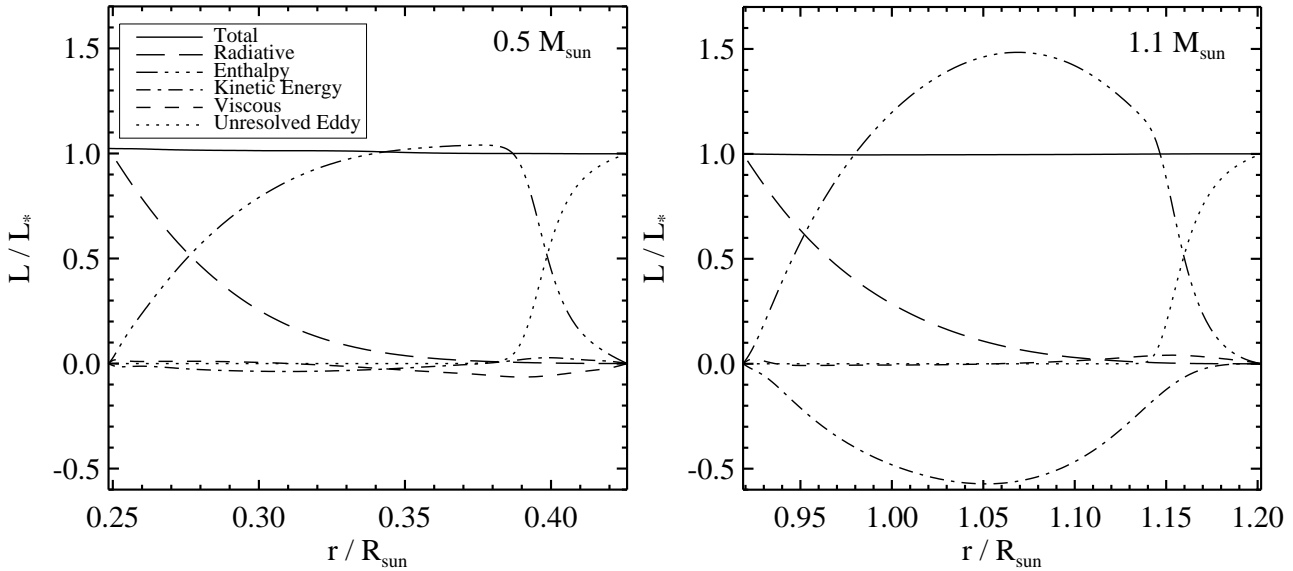


Fig. 4 Energy flow in 0.5 (left) and $1.1 M_{\odot}$ (right) cases as a function of radius in the computational domain. Shown are the spherically- and time-averaged luminosities, after the simulations have reached a statistical steady-state.

In each case, we chose the viscosity at the outer part of the domain, ν_{top} , in order to ensure that the resulting convective turbulence has a significant Reynolds number. As shown in section 3, a higher stellar luminosity leads to larger convective velocities, and thus a larger viscosity is needed to keep the Reynolds numbers comparable (explaining the trend of ν_{top} apparent in table 2). Within the domain, the viscosity in each case depends only upon radius, and it varies as the inverse square root of the background density. Scaling the viscosity in this way ensures a significant turbulence level at all radii and is used in most previous ASH models in the literature. The thermal diffusivity κ equals 4ν everywhere in the domain, giving a constant Prandtl number of 0.25 for all cases. The rotation rate of the reference frame (Ω_0), which equals the rotation rate of the star, is set to the solar rate for all 4 stars.

The Rayleigh numbers (calculated using the steady-state value of the entropy in the simulations), Taylor numbers, and convective Rossby numbers for each case are also given in table 2. The Rayleigh and Taylor numbers, show a strong decrease with increasing stellar mass, which is primarily explained by the trend in the diffusivities. If the diffusivities were constant, these numbers would increase with mass for these stars. The convective Rossby number generally increases with mass, meaning that for the same rotation rate, the coriolis force has less influence on the dynamics.

2.3 Reaching a statistical steady-state and energy flux balance

At the start of the simulation, the star is in a quiescent state. Thus, there is no significant enthalpy flux, and the system is not initially in radial energy flux balance. In this situation, the evolution of the system, according to equations (1)–(3), ensures that the entropy gradient evolves toward an energy

flux balanced state. Furthermore, since the gas in the computational domain is unstably stratified ($\partial\bar{S}/\partial r < 0$), with a large Rayleigh number (see table 2), significant convective motions begin rapidly after the start of the simulations. Once vigorous convection begins, an energy flux balance is achieved within a few convective turnover times (months, typically) and maintained for the duration of the simulations. In this state, the net energy transport across the domain is constant at all radii, when averaged over several convective turnover times.

Figure 4 shows the spherically- and time-averaged luminosity, as a function of radius in the whole domain, for the highest and lowest mass stars in this study. These are shown after the simulated stars have evolved for several years from the initial state. The boundary conditions ensure a fixed radiative energy flux into the domain at the inner boundary and a fixed unresolved eddy flux out of the domain at the outer boundary, both with luminosities equal to that of the modeled stellar luminosity. Within the domain, the radiative energy flux is nonzero, but it decreases in importance with increasing radius in the convection zone. The enthalpy flux, associated with convective motions, carries the bulk of the remaining energy flux from the lower boundary, across the convection zone, to the outer boundary. Due to the asymmetry between broad, slow upflows and narrow, fast downflows, there is generally a net negative (downward) flux of kinetic energy in the convection zone (e.g., as in the right panel of Fig. 4; Cattaneo et al., 1991; Hurlburt et al., 1986). As a result, the steady-state enthalpy luminosity (dash-triple-dotted line) peaks at a value significantly larger than L_* , in order that the net energy flow across the convection zone is constant and equal to the stellar luminosity. As demonstrated by the two extreme cases in Figure 4, the presence of a super-luminal enthalpy flux is increasingly important with mass, in our 4 simulations. It is

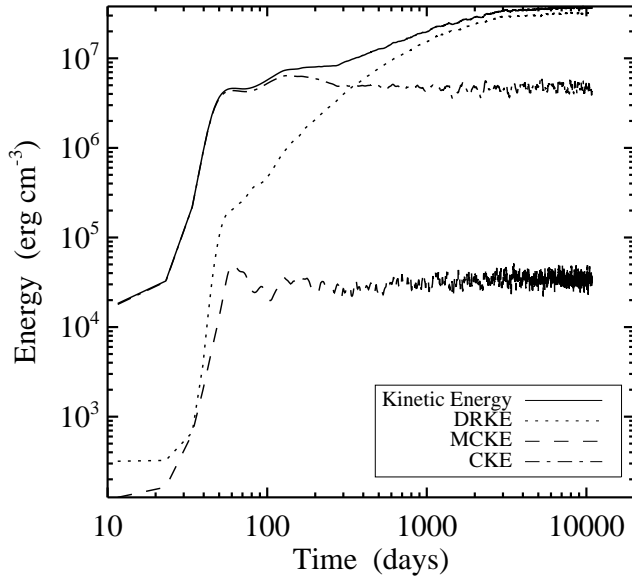


Fig. 5 Integrated kinetic energies in the domain, divided by the total volume, as a function of time, for the $0.5 M_{\odot}$ case. Shown are the kinetic energies associated with the differential rotation (DRKE), meridional circulation (MCKE), convective motions (CKE), and the total (solid line).

not clear whether this is due to an intrinsic property of the stars (such as the luminosity), or whether it only depends upon (e.g.) the viscosity, which is systematically different in each of our cases (table 2). However, it does seem that the faster flows found in the more massive stars (discussed below) yields a larger negative kinetic energy flux, since the difference between the broad-slow upflows and narrow-fast downflows is accentuated.

Although the energy flux balance is established relatively rapidly in the convection zone, the statistical properties of the turbulence can take longer to settle down, as they evolve in response to (e.g.) Reynolds stresses and the dissipation of energy on small scales. In addition, these systems typically exhibit global, axisymmetric flows such as differential rotation and meridional circulation. These flows are also influenced by the Reynolds stresses, and the meridional circulation typically has velocities smaller than the convective velocities. Thus, the global flows settle down on timescales of the order of 10 times the convective turnover time. In order to ensure the simulations have time to establish these global flows and are near their turbulent statistical steady-state, we have run each model for a timescale comparable to the global viscous dissipation timescale (L^2/ν).

As an example, Figure 5 shows the globally integrated kinetic energies in the $0.5 M_{\odot}$ case, as a function of time from the start of the simulation. The evolution during the first year is characterized by an initially linear (exponential) growth of the convective instability, followed by a non-linear saturation phase, then by relaxation oscillations until it settles down into a statistically steady state. The longer term evolution exhibits a growth in the differential rotation,

which also reaches a steady state. It is clear from Figure 5 that there is little change during the last 5000 days of evolution. The results in Figure 4 and presented below are shown during this mature state of the systems.

3 3D simulations

The ending time of each of the 4 simulations (t_f) is listed in table 3. In this section, we present the convective properties and the global flows existing in each case.

3.1 Properties of convection

Figure 6 shows the radial velocity on slices of constant radius at slightly below the top of the domain and at the middle of the domain, for the 0.5 (top), 0.7 (middle), and 1.1 (bottom) M_{\odot} cases. Also shown are the slices of temperature at the middle of the domain (right panels). The temperature slices generally appear less structured than the radial velocity slices because the Prandtl number is less than unity (0.25), so that the thermal diffusivity (κ) is larger than the kinematic viscosity (ν).

The convective patterns and characteristic eddy sizes are influenced strongly by the density scale height, as well as by the contrast between horizontal and vertical velocity (see, e.g., Bessolaz & Brun, 2011). Near the surface, where the density scale height is smallest, the shell slices exhibit typical convective patterns characterized by hot, broad/patchy upflows surrounded by cool, narrow downflow lanes (e.g., Cattaneo et al., 1991; Miesch et al., 2008). Deeper in the convection zone, the downflow lanes often merge and generally lose their connectivity with respect to the surface patterns, and the convection has a less patchy appearance. The near-surface shell slices (left panels of Fig. 6) are shown at a location where the unresolved eddy flux dominates the other fluxes (see Fig. 4). The unresolved eddy flux is a spherically symmetric quantity, and it does not affect the shape of the convective patterns, but it does influence the level of (resolved) turbulence, since the unresolved eddy flux reduces the convective driving. However, at the location of the near-surface shell slices shown, all cases are still turbulent, with a significant convective (enthalpy) flux and Reynolds numbers in the range of 10 – 30.

In all of our cases, the convective patterns evolve on typical timescales of a few weeks to a few months, with cells merging, splitting, and disappearing. The evolution of the convective motions in the $1.1 M_{\odot}$ case generally evolve on timescales of a factor of a few times shorter than in the $0.5 M_{\odot}$ case. The convective patterns are partly advected by the local shear and, depending on whether the flow is prograde or retrograde, are tilted to the right or the left near the equator. At higher latitude, beyond the tangent cylinder (an imaginary circle crossing the upper surface with a cylindrical radius of R_{cz}), the convective cells are less aligned with the rotation axis and exhibit a more patchy behavior.

Table 3 Simulation results for each case. The amount of evolution time since the start of the simulation is denoted t_f . Temporal averages of the rms components of velocity \tilde{v}_r , \tilde{v}_ϕ , \tilde{v}_θ , speed \tilde{v} , and fluctuating velocities \tilde{v}'_ϕ and \tilde{v}' are evaluated at the midlevel of the domain and given in units of m s^{-1} . The temporally averaged rms temperature fluctuation at midlevel is \tilde{T} . Also listed are the rms Reynolds number $\tilde{R}_e \equiv \tilde{v}'L/\nu$, Rossby number $\tilde{R}_o \equiv \tilde{v}'/(2\Omega_0L)$, and Péclet number $\tilde{P}_e \equiv \tilde{v}'L/\kappa$, evaluated at the midlevel, and the convective turnover timescale $\tau_{\text{to}} \equiv L/\tilde{v}_r$. The $\Delta\Omega$ is the difference in angular rotation rate at the outer boundary, between latitudes of 0° and 60° . The ΔT is the difference in the temporally and azimuthally averaged temperature at the base of the convection zone (R_{cz}), between latitudes of 60° and 0° . Finally, \tilde{v}_{mc} is the rms meridional circulation speed, calculated from temporally and azimuthally averaged poloidal velocity and by taking the rms of all values at a constant midlevel radius.

Mass (M_\odot)	t_f (years)	\tilde{v}_r (m/s)	\tilde{v}_θ (m/s)	\tilde{v}_ϕ (m/s)	\tilde{v}'_ϕ (m/s)	\tilde{v} (m/s)	\tilde{v}' (m/s)	\tilde{T} (K)	\tilde{R}_e	\tilde{R}_o	\tilde{P}_e	τ_{to} (days)	$\Delta\Omega/\Omega_0$ (%)	ΔT (K)	\tilde{v}_{mc} (m/s)
0.5	30	8.7	9.8	37	9.3	40	16	0.22	309	0.025	77	164	37	0.61	0.29
0.7	28	20	21	74	21	79	36	0.76	139	0.049	35	82	41	2.2	0.64
0.9	22	47	45	95	50	115	82	1.3	151	0.094	38	41	30	3.6	1.5
1.1	8.6	150	134	242	136	314	241	6.1	133	0.24	33	15	-42	-9.9	22

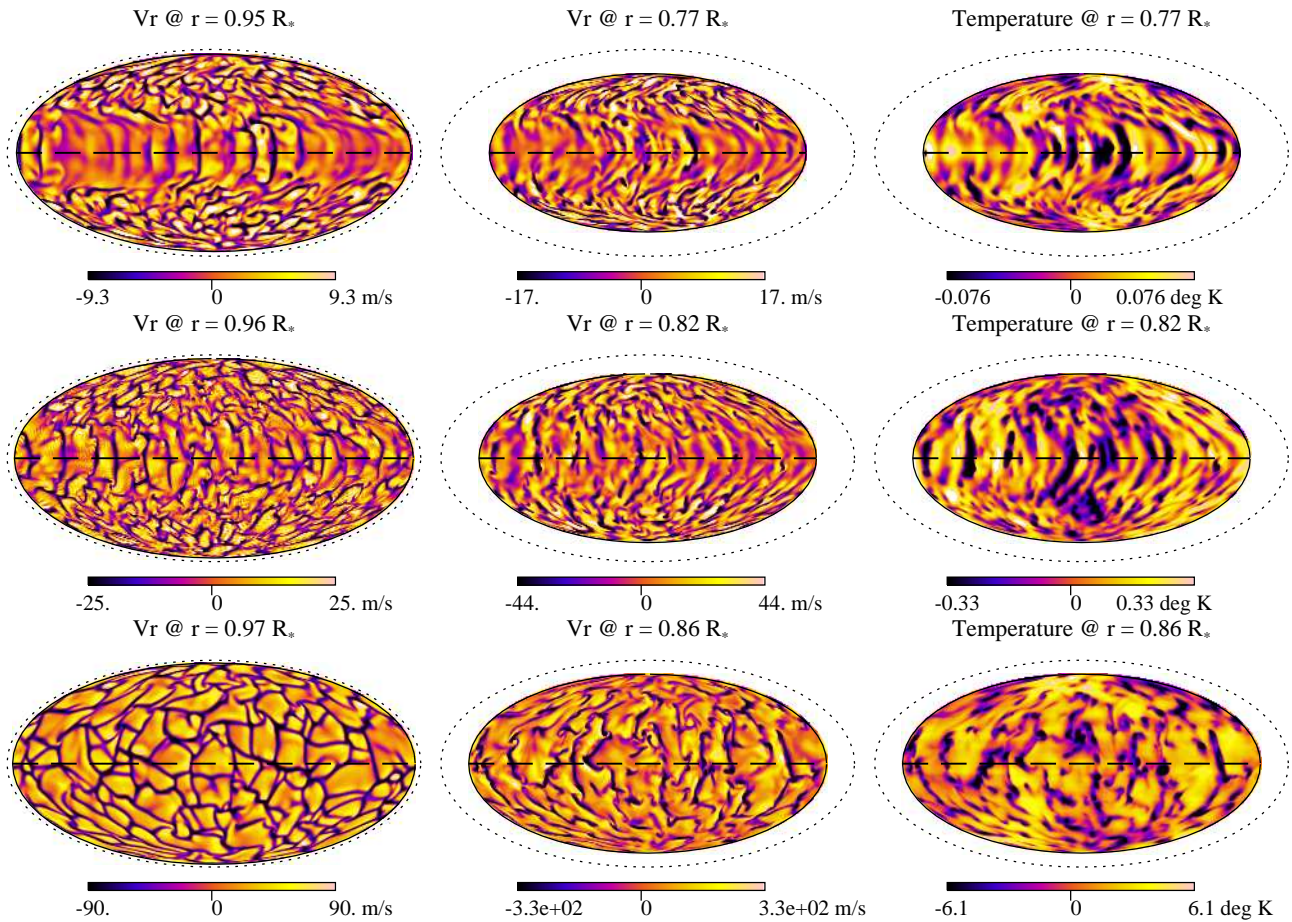


Fig. 6 Slices at constant radius (Mollweide view) for the $0.5 M_\odot$ case (top), $0.7 M_\odot$ case (middle), and $1.1 M_\odot$ case (bottom), showing the radial velocity near the surface (left panels) and in the midlevel (middle panels) of the domain and the temperature at midlevel (right panels). In the temperature slices, the azimuthal average has been subtracted, to emphasize the temperature fluctuations. The dotted line corresponds to the stellar surface and the dashed line to the equator.

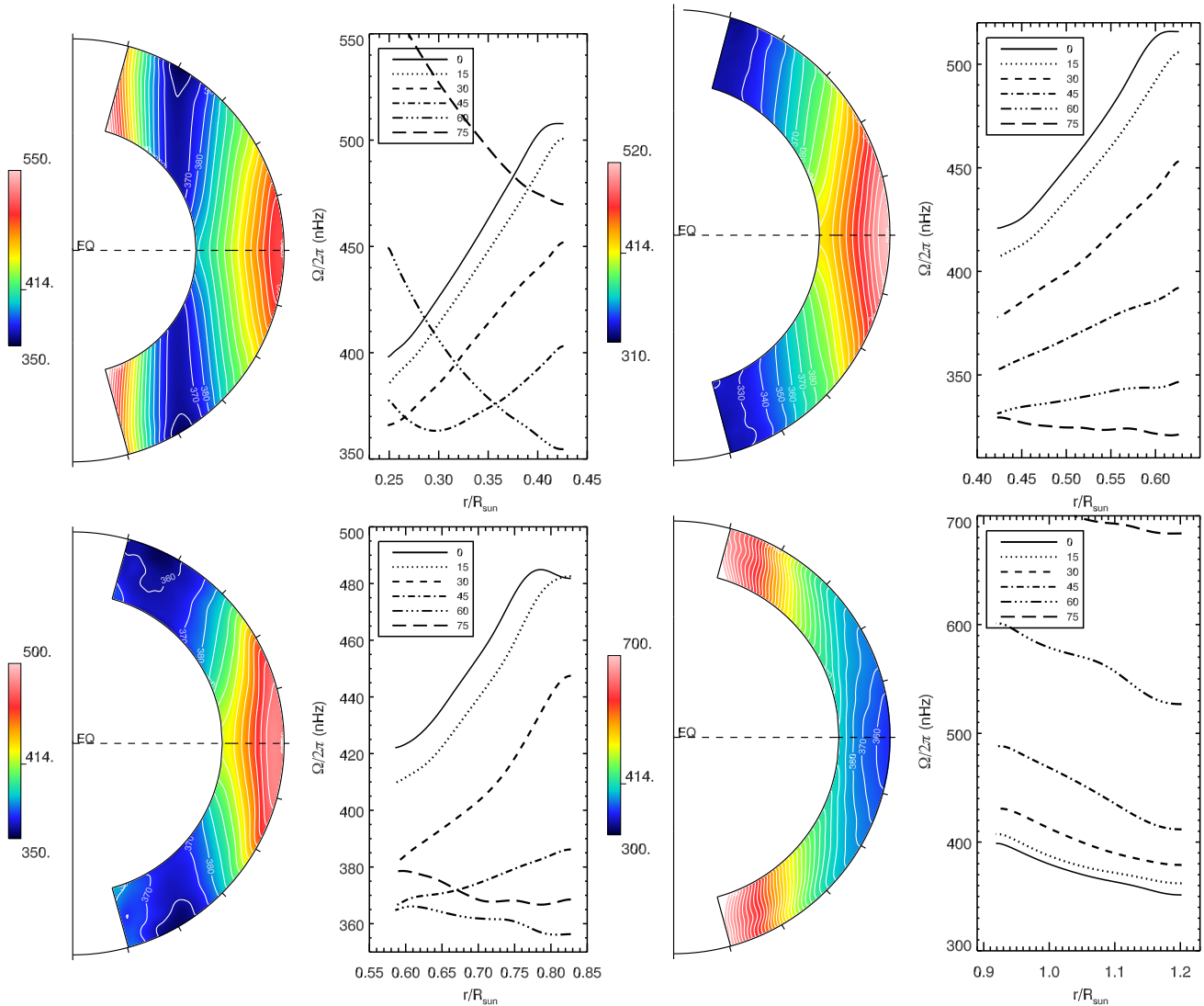


Fig. 7 Azimuthally and temporally averaged Rotation frequency in a meridional slice through the domain (contour/color plots; rotation axis is vertical) and shown along radial lines at different latitudes (line plots, latitude given in degrees). Shown are the 0.5 (top left), 0.7 (top right), 0.9 (bottom left), and 1.1 (bottom right) M_{\odot} cases.

As evident in the Figure, the 0.5 M_{\odot} case exhibits convective patterns near the equatorial region that are inhomogeneous, consisting of vigorous convection over some range of longitudes and relatively quiescent regions at other longitudes. Such “active nest” convective patterns have been discussed by Ballot et al. (2007) and Brown et al. (2008) and are likely related to our choice of low Prandtl number. The remaining 3 cases, exhibit vigorous convection within the entire volume of the convection zone, as seen for the 0.7 and 1.1 M_{\odot} cases shown in the bottom two rows of Figure 6.

Table 3 lists the rms velocities at the middle of the computational domain for each case. There is a clear trend of increasing convective velocities with increasing stellar mass. As evident in the right panels of Figure 6 and in the values of the rms temperature (\bar{T}) listed in table 3, there is also a strong trend of increasing temperature contrast between up-

and downflows, with increasing mass. This trend is steeper if one considers the temperature fluctuation relative to the mean temperature, since the mean background temperature in the 1.1 M_{\odot} convection zone midlevel is ~ 3 times colder than for the 0.5 M_{\odot} star (see §2.1). Furthermore, the average mass density in the convective envelope decreases with increasing stellar mass (the midlevel density in the 1.1 M_{\odot} case is 280 times lower than in the 0.5 M_{\odot} case), which decreases the efficiency of convective energy transport. In spite of the lower density, the convection in higher mass stars is able to carry a larger luminosity than the lower mass stars, due to a combination of larger stellar radii, higher convective velocities, and higher temperature contrasts between up- and downflows.

Table 3 also lists the Reynolds, Rossby, and Péclet numbers for each model. The Reynolds (and Péclet) have a range of a factor of a few, with no trend in mass. These values pri-

marily reflect our choice of ν_{top} for each case (tab. 2) rather than any intrinsic property of the stars. For our choices of ν_{top} , the $0.5 M_{\odot}$ case has the highest Reynolds number. On the other hand, the Rossby numbers do not depend strongly on our choice of diffusivities, and they show a strong dependence on mass, primarily due to the trend in convective velocity with mass, at a constant rotation period. Finally, table 3 lists a characteristic convective turnover timescale for each case. This also shows a strong trend with mass, primarily due to the trend in convective velocities.

3.2 Differential rotation and meridional circulation

Figure 7 shows the differential rotation in all 4 cases. The 2D plots in the Figure exhibit isorotation contours that are nearly aligned on cylinders in all cases. This behavior is typical for simulations such as these that have no enhanced latitudinal entropy gradient present at the lower boundary of the convection zone (Ballot et al., 2007; Miesch et al., 2006).

The angular rotation rate in the $0.5 M_{\odot}$ case has a minimum value at mid latitudes, a local maximum in the outer equatorial region, and a global maximum near the pole. A similarly “banded” differential rotation pattern is evident in a number of previously published ASH simulations (e.g. Bessolaz & Brun, 2011; Browning, 2008). The differential rotation in the 0.7 and $0.9 M_{\odot}$ cases are the most solar-like, with the fastest angular rotation rate at the equator and slowest at higher latitudes. However, the $1.1 M_{\odot}$ case exhibits anti-solar rotation, where the slowest angular velocity is at the equator. A reversal of the sense of differential rotation was also observed in the simulations of Bessolaz & Brun (2011) to be an effect of the thickness of the convection zone. In that study, the stellar structure and luminosity was held fixed, while only the thickness of the convection zone was varied. The thickness of the convection zone in our $1.1 M_{\odot}$ case (as a fraction of R_*) is comparable to the models of Bessolaz & Brun (2011) showing anti-solar rotation. This would suggest that the switch from solar to anti-solar may have more to do with convection zone thickness than with stellar structural properties. At the same time, our choice of parameters may also have influenced this outcome. In particular, the $1.1 M_{\odot}$ case has the largest Rossby numbers (see tabs. 2 and 3), which means that the convection is less influenced by rotation than in the other cases.

Each case exhibits a time-averaged, axisymmetric, latitudinal temperature gradient. For the 3 highest mass cases, this is characterized by a monotonic change from equator to pole. The $1.1 M_{\odot}$ case has a hotter equator, while the 0.7 and $0.9 M_{\odot}$ cases have hotter poles (as in the sun). The $0.5 M_{\odot}$ case has a more complex temperature pattern with a maximum at mid latitudes, while the latitudinal entropy gradient in all cases follows a more monotonic behavior from equator to pole. The second-to-last column of table 3 shows the temporally and azimuthally averaged temperature difference between the equator and a latitude of 60° , at the base of the convection zone. It is evident that the temperature

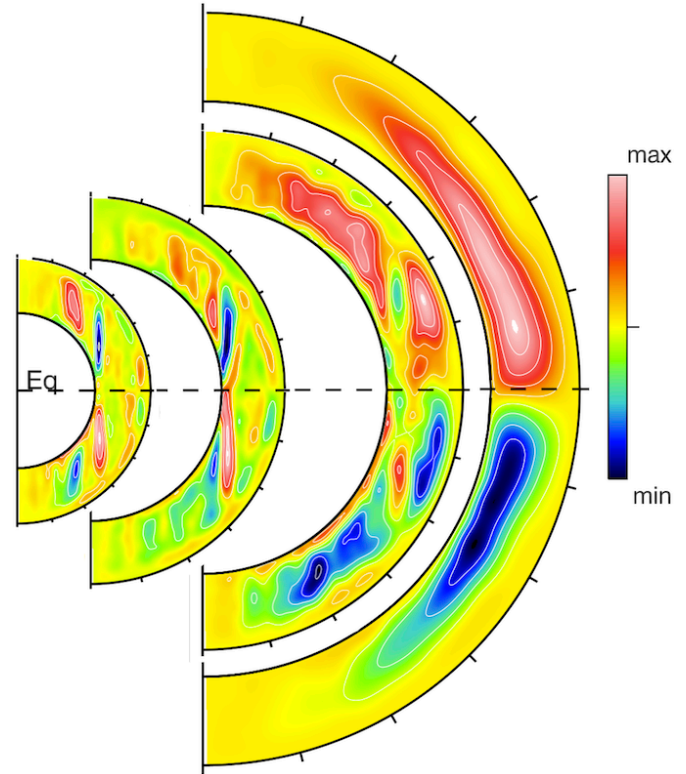


Fig. 8 Contours of the stream function of the meridional flow for the 0.5 , 0.7 , 0.9 , and $1.1 M_{\odot}$ cases (left to right), where the physical sizes of the stars are shown to scale. The contours follow streamlines in the meridional plane from temporally and azimuthally averaged data. The colors indicate clockwise (blue) and counter-clockwise (red) circulation, and the stellar rotation axis is vertical.

gradients are steeper for higher mass stars. The more complex temperature structure of the lowest mass case is consistent with the banded differential rotation pattern, and the reversed polarity of the temperature variation in the highest mass case is consistent with anti-solar differential rotation.

The fractional differential rotation of each case, measured at the top of the domain between latitudes 0 and 60 degrees, is listed in the final column of table 3. These values of $\Delta\Omega/\Omega_0$ in the table, show that the magnitude of the differential rotation ranges from 30 to 42% for all cases.

Figure 8 shows the meridional circulation for all 4 cases. The plots are shown to scale, according to the physical size of each of the stars. For the 2 highest mass stars, the circulation pattern is dominated by a global, unicellular flow pattern from equator to pole near the surface and from pole to equator near the base of the convection zone. However, as evident in the Figure, there is a trend for this flow to break up into a multi-cellular network of circulation patterns roughly aligned on cylinders, for the lower mass stars. The tendency for the meridional flow to breakup in this way for increasing convection zone depth was also seen in the simulations of Bessolaz & Brun (2011), suggesting that this

effect is mostly due to the size of the convection zone, rather than with other stellar properties.

The last column of table 3 shows the characteristic meridional circulation flow speed evaluated at the midlevel of the domain for each case. As with the convective velocities, there is a clear trend of increasing meridional circulation flow speed with increasing stellar mass. A similar trend is also seen in 2D models (e.g., Küker & Rüdiger, 2008). Since the physical size of the circulating patterns (evident in Fig. 8) also increases strongly with mass, this suggests that the characteristic timescale for these circulations is not strongly dependent on stellar mass. The values listed in table 3 also suggest that the ratio of the meridional circulation speed to the convection speed (e.g., $\tilde{v}_{\text{mc}}/\tilde{v}$) range from 2% for the 3 lowest mass stars to 9% for the $1.1 M_{\odot}$ case.

4 Summary & discussion

We have presented results from 3D dynamical simulations of the convection zones of 4 sun-like stars, spanning a mass range from 0.5 to $1.1 M_{\odot}$ and rotating at the solar rate. As presented in section 2.1, these stars cover a range in luminosities of a factor of 40 and have convection zone masses ranging from 18% to 1.1% of a solar mass. The physical sizes of the convection zones increase slightly with mass (ranging from 19% to 31% of a solar radius), although the fractional size decreases with mass (ranging from 44% to 24% of a stellar radius).

We found that the convective velocities and temperature contrast between up- and downflows is a strong function of mass. This is due to the strong luminosity dependence on mass, coupled with the fact that higher mass stars have less dense convective envelopes and thus require more vigorous convection. As a consequence of the trend in convective velocities, the Rossby number (for a constant Ω_0) increases and the convective turnover time decreases significantly with increasing mass.

The convective pattern in the $0.5 M_{\odot}$ case exhibits “active nests” on a finite range of longitudes in the equatorial region. The presence of these active nests appears to be related to both the Rossby and Prandtl numbers, in a sense that they have been seen in simulations with low R_o number and with $P_r = 0.25$ (Ballot et al., 2007; Brown et al., 2008) but not in cases with $P_r = 1.0$ (Ballot et al., 2007; Bessolaz & Brun, 2011). This may be due to the relative amplitude of the local shear, which tends to be stronger for lower P_r . Stronger shear disrupts convective motions and can locally inhibit radial motions.

The angular rotation rate has a peak value at the surface and equator for the 0.5, 0.7, and $0.9 M_{\odot}$ cases. However, our simulations exhibit a differential rotation that is “banded,” with a minimum at mid latitudes and another maximum at the poles, for the $0.5 M_{\odot}$ case. The 0.7 and $0.9 M_{\odot}$ cases exhibit the most solar-like differential rotation, with a maximum at the equator and minimum near the poles, but the $1.1 M_{\odot}$ case exhibits anti-solar differential rotation. The

magnitude of the differential rotation is comparable in all cases.

The 4 simulations presented here exhibit isorotation contours that are nearly aligned on cylinders, approximately following the Taylor-Proudman constraint. From simulations of the solar convection zone (e.g., Miesch et al., 2006), we know that the Taylor-Proudman constraint can be broken by a thermal wind driven by very small latitudinal gradients of temperature or entropy, with differences of a few Kelvin sufficing to move cylindrical profiles to radially-aligned rotation profiles. Such gradients and thermal winds do occur in the simulations presented here, but the presence of the domain boundary at the base of the convection zone somewhat inhibits this effect. By moving the lower domain boundary deep into the radiation zone, Brun et al. (2011) demonstrated that the presence of a dynamically self-consistent tachocline alleviates the effects of the lower boundary on the convection zone dynamics and results in a stronger thermal wind, isorotation contours more aligned to the radial direction, and more realistic meridional circulations and convective penetration. In future work, similar models will be developed for the stars in the present study.

The meridional circulation is dominated by a single, global circulation pattern in each hemisphere for the most massive cases, but breaks up into smaller scale patterns, aligned with the cylindrical z-direction, for lower mass stars.

Future work with these models should explore cases that include, for example, (a) a part of the radiation zone in the computational domain, in order to determine how the presence of a tachocline affects the convection zone properties, (b) the effects of different rotation rates, in particular faster rotation, to understand how the properties of these stars differ at younger ages, and (c) magnetic fields, in order to address the magnetic dynamo properties of these stars.

Acknowledgements. SPM, ODC, and ASB were supported by the ERC through grant 207430 STARS2. BPB is supported in part by NSF Astronomy and Astrophysics postdoctoral fellowship AST 09-02004. CMSO is supported by NSF grant PHY 08-21899.

References

- Baliunas, S. L., Donahue, R. A., Soon, W. H., Horne, J. H., Frazer, J., Woodard-Eklund, L., Bradford, M., Rao, L. M., Wilson, O. C., Zhang, Q., Bennett, W., Briggs, J., Carroll, S. M., Duncan, D. K., Figueroa, D., Lanning, H. H., Misch, T., Mueller, J., Noyes, R. W., Poppe, D., Porter, A. C., Robinson, C. R., Russell, J., Shelton, J. C., Soyumer, T., Vaughan, A. H., & Whitney, J. H. 1995, *Astrophysical Journal*, 438, 269
- Ballot, J., Brun, A. S., & Turck-Chièze, S. 2007, *The Astrophysical Journal*, 669, 1190
- Barnes, J. R., Cameron, A. C., Donati, J.-F., James, D. J., Marsden, S. C., & Petit, P. 2005, *Monthly Notices of the Royal Astronomical Society: Letters*, 357, L1
- Bessolaz, N. & Brun, A. S. 2011, *The Astrophysical Journal*, 728, 115
- Brown, B. P. 2009, Ph.D. Thesis, 1
- Brown, B. P., Browning, M. K., Brun, A. S., Miesch, M. S., & Toomre, J. 2008, *The Astrophysical Journal*, 689, 1354

- Brown, B. P., Miesch, M. S., Browning, M. K., Brun, A. S., & Toomre, J. 2011, *The Astrophysical Journal*, 731, 69
- Browning, M. K. 2008, *The Astrophysical Journal*, 676, 1262
- Browning, M. K., Brun, A. S., & Toomre, J. 2004a, *The A-Star Puzzle*, 224, 149, ISBN: 0521850185
- . 2004b, *The Astrophysical Journal*, 601, 512
- Browning, M. K., Miesch, M. S., Brun, A. S., & Toomre, J. 2006, *The Astrophysical Journal*, 648, L157
- Brun, A. S., Miesch, M., & Toomre, J. 2011, *Astrophysical Journal*, in press
- Brun, A. S., Miesch, M. S., & Toomre, J. 2004, *The Astrophysical Journal*, 614, 1073
- Brun, A. S. & Palacios, A. 2009, *The Astrophysical Journal*, 702, 1078
- Brun, A. S. & Toomre, J. 2002, *The Astrophysical Journal*, 570, 865
- Cattaneo, F., Brummell, N. H., Toomre, J., Malagoli, A., & Hurlburt, N. E. 1991, *Astrophysical Journal*, 370, 282
- Clune, T. L., Elliott, J. R., Glatzmaier, G. L., Miesch, M. S., & Toomre, J. 1999, *Parallel Comput.*, 25, 361
- DeRosa, M., Gilman, P. A., & Toomre, J. 2002, *The Astrophysical Journal*, 581, 1356
- Donahue, R. A., Saar, S. H., & Baliunas, S. L. 1996, *Astrophysical Journal* v.466, 466, 384
- Donati, J.-F., Cameron, A. C., & Petit, P. 2003, *Monthly Notices of the Royal Astronomical Society*, 345, 1187
- Featherstone, N. A., Browning, M. K., Brun, A. S., & Toomre, J. 2009, *The Astrophysical Journal*, 705, 1000
- Hurlburt, N. E., Toomre, J., & Massaguer, J. M. 1986, *Astrophysical Journal*, 311, 563
- Küker, M. & Rüdiger, G. 2008, *Journal of Physics: Conference Series*, 118, 2029
- Lovis, C., Dumusque, X., Santos, N. C., Bouchy, F., Mayor, M., Pepe, F., Queloz, D., Ségransan, D., & Udry, S. 2011, eprint arXiv, 1107, 5325, 25 pages, 19 figures, submitted to A&A
- Miesch, M. S., Brun, A. S., Rosa, M. L. D., & Toomre, J. 2008, *The Astrophysical Journal*, 673, 557
- Miesch, M. S., Brun, A. S., & Toomre, J. 2006, *The Astrophysical Journal*, 641, 618
- Morel, P. 1997, *A & A Supplement series*, 124, 597
- Oláh, K., Kolláth, Z., Granzer, T., Strassmeier, K. G., Lanza, A. F., Järvinen, S., Korhonen, H., Baliunas, S. L., Soon, W., Messina, S., & Cutispoto, G. 2009, *Astronomy and Astrophysics*, 501, 703
- Petit, P., Dintrans, B., Solanki, S. K., Donati, J.-F., Aurière, M., Lignières, F., Morin, J., Paletou, F., Velez, J. R., Catala, C., & Fares, R. 2008, *Monthly Notices of the Royal Astronomical Society*, 388, 80
- Pizzolato, N., Maggio, A., Micela, G., Sciortino, S., & Ventura, P. 2003, *Astronomy and Astrophysics*, 397, 147
- Saar, S. H. & Brandenburg, A. 1999, *The Astrophysical Journal*, 524, 295
- Strassmeier, K. G., Fekel, F. C., Bopp, B. W., Dempsey, R. C., & Henry, G. W. 1990, *Astrophysical Journal Supplement Series* (ISSN 0067-0049), 72, 191
- Verner, G. A., Elsworth, Y., Chaplin, W. J., Campante, T. L., Corsaro, E., Gaulme, P., Hekker, S., Huber, D., Karoff, C., Mathur, S., Mosser, B., Appourchaux, T., Ballot, J., Bedding, T. R., Bonanno, A., Broomhall, A.-M., García, R. A., Handberg, R., New, R., Stello, D., Régulo, C., Roxburgh, I. W., Salabert, D., White, T. R., Caldwell, D. A., Christiansen, J. L., & Fanelli, M. N. 2011, *Monthly Notices of the Royal Astronomical Society*, 415, 3539
- Wright, N. J., Drake, J. J., Mamajek, E. E., & Henry, G. W. 2011, eprint arXiv, 1109, 4634